Optical Absorption and Emission Mechanisms of Single Defects in Hexagonal Boron Nitride

Nicholas R. Jungwirth and Gregory D. Fuchs*
Cornell University, Ithaca, New York 14853, USA
(Received 25 April 2017; published 31 July 2017)

We investigate the polarization selection rules of sharp zero-phonon lines (ZPLs) from isolated defects in hexagonal boron nitride (HBN) and compare our findings with the predictions of a Huang-Rhys model involving two electronic states. Our survey, which spans the spectral range ~550–740 nm, reveals that, in disagreement with a two-level model, the absorption and emission dipoles are often misaligned. We relate the dipole misalignment angle ($\Delta\theta$) of a ZPL to its energy shift from the excitation energy (ΔE) and find that $\Delta\theta \approx 0°$ when ΔE corresponds to an allowed HBN phonon frequency and that $0° \leq \Delta\theta \leq 90°$ when ΔE exceeds the maximum allowed HBN phonon frequency. Consequently, a two-level Huang-Rhys model succeeds at describing excitations mediated by the creation of one optical phonon but fails at describing excitations that require the creation of multiple phonons. We propose that direct excitations requiring the creation of multiple phonons are inefficient due to the low Huang-Rhys factors in HBN and that these ZPLs are instead excited indirectly via an intermediate electronic state. This hypothesis is corroborated by polarization measurements of an individual ZPL excited with two distinct wavelengths that indicate a single ZPL may be excited by multiple mechanisms. These findings provide new insight on the nature of the optical cycle of novel defect-based single-photon sources in HBN.

DOI: 10.1103/PhysRevLett.119.057401

Wide band gap semiconductors host point defects, or color centers, that can feature optical and spin properties that are useful for applications in quantum optics, precision sensing, and quantum information technology [1–5]. Some color centers, such as the nitrogen vacancy center in diamond [6–11], are bright enough to be investigated in the single defect limit using single-molecule microscopy techniques [12,13]. While diamond is the most celebrated host material, the last several years have witnessed the discovery of defect-based single-photon sources in SiC [1,14–20], ZnO [21–26], GaN [27], WSe_2 [28–30], WS_2 [31], and hexagonal boron nitride (HBN) [32–45]. The latter three materials exist as two-dimensional monolayers and layered solids, thus offering the possibility of integrating single-photon sources with van der Waals heterostructure devices for tuning and other control. Defect emission in HBN can be ultrabright [32], have a narrow linewidth [33], be tuned [39], and remain photostable up to 800 K [41]. These positive attributes have sparked strong interest in HBN defects from research groups around the world [32–45]. Despite this surge of interest, most works have focused on characterizing the phenomenology of HBN emission, leaving open several difficult-to-answer questions regarding the fundamental nature of HBN quantum emitters. These include the structural origin of the defect(s) responsible for single-photon emission, the reason(s) for the broad distribution of zero-phonon line (ZPL) energies (E_{ZPL}), the spin properties, and the physical mechanism(s) involved in the defect's optical cycle.

In this work we address the transition mechanism(s) involved in the defect's optical cycle. We perform spectrally resolved polarization measurements of optical absorption and emission at cryogenic temperatures and compare our findings with the predictions of a Huang-Rhys model. We find that when the energy difference between the exciting light and the ZPL is less than the maximum phonon energy in HBN, the defect's polarization properties are well explained by a Huang-Rhys model with two electronic states. Conversely, when this energy difference exceeds the maximum phonon energy, a Huang-Rhys model with two electronic states fails at explaining the observed behavior. These findings suggest that ZPL emission may be mediated by an intermediate electronic state. This explanation is supported by polarization measurements performed with lasers of different energies that verify that a single ZPL may be excited via multiple mechanisms. These effects, which have not been observed in another defect system, arise in HBN owing to the combination of a small Huang-Rhys factor (strong ZPL), large oscillator strength, and presence of many coupled electronic energy levels. Our findings, which provide new insight on the optical properties and level structure of HBN defects, are key for designing future experiments and applications.

The fundamental mechanism governing nonresonant absorption and emission from point defects has been known for some time [46] and is illustrated in the configuration coordinate diagram shown in Fig. 1(a). In the Huang-Rhys model, a defect may undergo incoherent transitions to and from an electronic ground state (μ) and an electronic excited state (μ^*) that are mediated by lattice phonons. Note that although only one phonon frequency ω, ω^* is depicted for

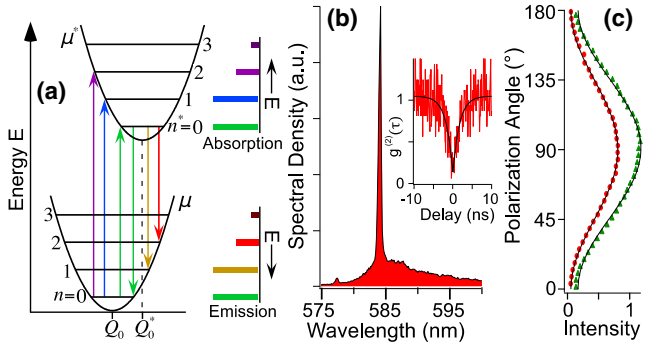

FIG. 1. (a) Configuration coordinate diagram with $S = 1$ illustrating phonon-mediated transitions to and from an electronic ground state μ and electronic excited state μ^* at zero temperature. While in electronic ground state μ with $n = 0$ phonons, the defect may absorb an optical photon and enter state (μ^*, n^*). Following rapid thermalization to the vibronic ground state the defect may radiatively relax from state $(\mu^*, 0)$ to (μ, n) with a probability given by the Frank-Condon factor. For linear modes ($\omega = \omega^*$) the absorption and emission bands, shown on the right, are mirror reflections of one another. (b) Emission spectrum of a defect revealing a sharp ZPL at ~584 nm. This ZPL corresponds to single-photon emission, as verified by the antibunching dip in $g^{(2)}(\tau)$ shown as an inset. (c) The polarization profiles for absorption (green triangles) and emission (red circles) are aligned, as predicted by the Huang-Rhys model in (a).

each electronic state μ, μ^*, the model is readily adapted to include additional phonon modes [47,48]. In the diagram, the horizontal axis corresponds to the nuclear coordinate Q that specifies the lattice configuration and the vertical axis corresponds to the total energy of the defect-lattice system. The zero-phonon lattice configuration in the excited state, $Q_0^* = \langle \mu^* | Q | \mu^* \rangle$, differs from that of the ground state, $Q_0 = \langle \mu | Q | \mu \rangle$, because each state produces a unique electrostatic potential. Each optical cycle begins with the system in the electronic state μ and a vibronic state occupation of n phonons, with a probability governed by the Bose-Einstein distribution. Following the absorption of an optical photon, the system rapidly thermalizes and the excited state μ^* with n^* phonons is occupied. In the Frank-Condon approximation, where the fast electronic rearrangement precedes the slower lattice relaxation, the transition rate from to (μ^*, n^*) to (μ, n) is proportional to

$$|\langle \mu | \boldsymbol{r} | \mu^* \rangle|^2 \left| \int dQ \phi^*_{\mu,n}(Q) \phi_{\mu^*,n^*}(Q) \right|^2, \tag{1}$$

where $\phi_{\alpha,m}(Q)$ is the m-phonon lattice wave function when the defect is in electronic state α. Emission into the ZPL corresponds with $n = n^*$ transitions, where no phonons are created or annihilated. All other transitions contribute to the phonon sideband.

In Eq. (1) the first factor is the dipole matrix element of the transition. This term determines the polarization selection rules for absorption and emission and is symmetric under time reversal. Consequently, the model predicts identical polarization properties for absorption and emission. Additionally, because the symmetry properties of μ and μ^* are determined by the defect's crystallographic point group, the transition dipoles are typically aligned parallel or perpendicular to distinct crystallographic directions. The second factor in Eq. (1), the Frank-Condon factor $F_n^{n^*}$, is the overlap integral between displaced harmonic oscillators. This term determines the line shape of the absorption and emission bands. For linear modes $\omega = \omega^*$ and

$$F_n^{n^*} = e^{-S} S^{n-n^*} \left(\frac{n^*!}{n!} \right) (L_{n^*}^{n-n^*}(S))^2, \tag{2}$$

where $L_{n^*}^{n-n^*}$ are the associated Laguerre polynomials and S is a measure of defect-lattice coupling called the Huang-Rhys factor. In natural units $S = \frac{1}{2} m_{\text{eff}} \omega (Q_0 - Q_0^*)^2$, where m_{eff} is the effective mass of the mode. Because Eq. (2) is symmetric under time reversal, the absorption and emission bands of a transition are mirror reflections of one another about E_{ZPL} for linear modes. At temperature $T = 0$ there are no thermal phonons and the zero-temperature Frank-Condon factors $F_n^0 = e^{-S} S^n / n!$ dominate. In this limit the number of phonons created in a radiative transition is Poisson distributed about an average value of S, and the relative spectral weight of the ZPL is e^{-S}, which is the zero-temperature Debye-Waller factor.

To test the success of the Huang-Rhys model at describing the optical properties of isolated HBN defects we performed polarization spectroscopy using a house-built confocal microscope [25] (see Supplemental Material [49]). Figure 1(b) is a $T = 5$ K emission spectrum of a defect that reveals the presence of a narrow ZPL at ~584 nm. The two-photon correlation function, $g^{(2)}(\tau)$, of the collected photons (inset) possesses an antibunching dip at $\tau = 0$ extending well below 0.5, verifying that the ZPL corresponds to single-photon emission from a single defect transition. To investigate the polarization properties of absorption, we rotate the polarization of the exciting light and monitor the total fluorescence intensity. The result of this absorption measurement is shown as the green triangles in Fig. 1(c). Fixing the polarization of the exciting light to maximize the fluorescence, we determine the polarization of the emitted photons using a polarization analyzer placed in the collection path of the microscope [Fig. 1(c), red circles]. The solid lines are best fits using the equation

$$A + B \cos^2 \left(\frac{\pi}{180} (\theta - \langle \theta \rangle) \right), \tag{3}$$

where $\langle \theta \rangle$ is the spectrally averaged orientation of the absorption or emission dipole. As predicted by Eq. (1), we find that the maxima of absorption and emission are aligned for this defect. Additionally, we have shown previously that the temperature dependence of the ZPL intensity in HBN is well modeled by the temperature-dependent Debye-Waller factor [33]. Thus, we conclude that the

Huang-Rhys model is a good description of the observed properties for the defect shown in Figs. 1(b) and 1(c).

A survey of ZPLs in HBN reveals that, in contrast to the data shown in Figs. 1(b) and 1(c), the absorption dipole is frequently not aligned parallel to the emission dipole. To verify that the misalignment we observe is not an experimental artifact resulting from the wavelength- and polarization-dependent retardances introduced by optical elements in the microscope, we performed spectrally resolved polarization measurements (see Supplemental Material [49]). For absorption we vary the polarization of the exciting light and record an emission spectrum at each angle. This measurement produces $I_{\mathrm{abs}}(\theta, E)$, where $I_{\mathrm{abs}}(\theta, E)\delta E$ is the number of photons collected in the energy range $(E, E+\delta E)$ when the exciting light is polarized at θ. For each energy E' we fit $I_{\mathrm{abs}}(\theta, E')$ to Eq. (3) to obtain $\theta_{\mathrm{abs}}(E')$, which is the polarization angle that maximizes $I_{\mathrm{abs}}(\theta, E)$ when $E = E'$. For the emission measurement, we fix the exciting light polarization to $\theta_{\mathrm{abs}}(E_{\mathrm{ZPL}})$ and record an emission spectrum for a series of positions of the polarization analyzer in the collection path. In an analogous fashion to the absorption case we obtain $I_{\mathrm{emit}}(\theta, E)$ and $\theta_{\mathrm{emit}}(E)$ for the emitted light. We apply a calibration to $\theta_{\mathrm{emit}}(E)$ to correct for wavelength- and polarization-dependent retardances (see Supplemental Material [49]) introduced by the collection path of the confocal microscope.

Figure 2(a) is a two-dimensional image plot of $I_{\mathrm{emit}}(\theta, E)$ for a single defect with a ZPL at 2.06 eV (603 nm) that is excited by 2.33 eV (532 nm) light. The red trace in Fig. 2(b) is the unpolarized emission spectrum, $I_{\mathrm{emit}}(E)$, obtained by vertically summing the columns in the two-dimensional image. The one- and two-optical-phonon sidebands are evident at ~1.88 and ~1.7 eV, respectively, corresponding to a phonon energy of ~180 meV. The red circles in Fig. 2(c) are the spectrally averaged polarization of the emitted light, $I_{\mathrm{emit}}(\theta)$, obtained by horizontally summing the rows in the two-dimensional image. Lastly, the red trace in Fig. 2(a) corresponds to the calibrated $\theta_{\mathrm{emit}}(E)$ and indicates that, consistent with Eq. (1), the polarization state of photons emitted into the ZPL is the same as for those emitted into the phonon sideband. We also measured $I_{\mathrm{abs}}(\theta, E)$ (data not shown) and have included $\theta_{\mathrm{abs}}(E)$ as the green trace in Fig. 2(a). This trace indicates that the ZPL and phonon sideband intensities are maximized by the same polarization angle of the exciting light. However, in disagreement with Eq. (1), the absorption and emission dipoles are not aligned (e.g., $\Delta\theta = |\theta_{\mathrm{emit}}(E_{\mathrm{ZPL}}) - \theta_{\mathrm{abs}}(E_{\mathrm{ZPL}})| \neq 0$), suggesting that additional processes may be involved in this defect's optical cycle.

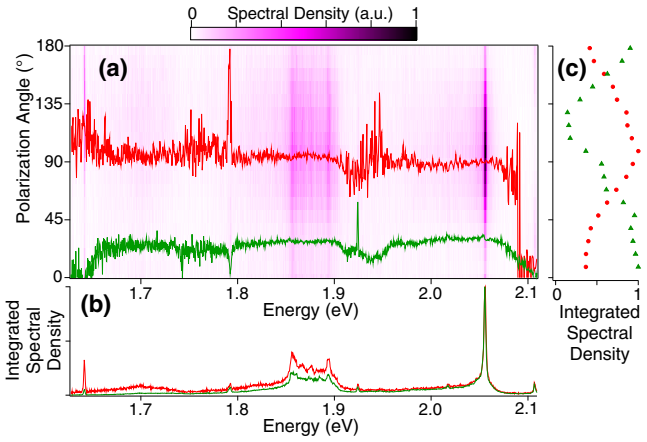

FIG. 2. (a) Two-dimensional image plot of $I_{\mathrm{emit}}(\theta, E)$ with a ZPL at ~2.06 eV. The average polarization of photons emitted with energy E, $\theta_{\mathrm{emit}}(E)$, is shown as the red trace. The unpolarized emission spectrum $I_{\mathrm{emit}}(E)$ and the spectrally averaged polarization profile $I_{\mathrm{emit}}(\theta)$, obtained by integrating the columns and rows of (a), are included as the red data in (b) and (c), respectively. The green data in (a)–(c) are the analogous measurements for absorption, obtained from $I_{\mathrm{abs}}(\theta, E)$ (not shown). In contrast to Fig. 1(c), $\theta_{\mathrm{emit}}(E_{\mathrm{ZPL}}) \neq \theta_{\mathrm{abs}}(E_{\mathrm{ZPL}})$.

To better understand the failure of the model we measured $\Delta\theta$ for 103 ZPLs distributed across the region 550–740 nm. For each ZPL investigated we verified $g^{(2)}(0) < 0.5$. Figure 3(a) is a scatter plot relating the dipole misalignment $\Delta\theta$ of a ZPL to its energy shift from the exciting light, defined as $\Delta E = E_{\mathrm{exc}} - E_{\mathrm{ZPL}}$, where E_{exc} is the energy of the exciting light. When ΔE is less than ~200 meV the data points are clustered near small values of $\Delta\theta$, as predicted by the Huang-Rhys model. Conversely, when ΔE exceeds ~200 meV the data points are broadly distributed between 0° and 90°. Therefore, ~200 meV corresponds to a critical energy shift above

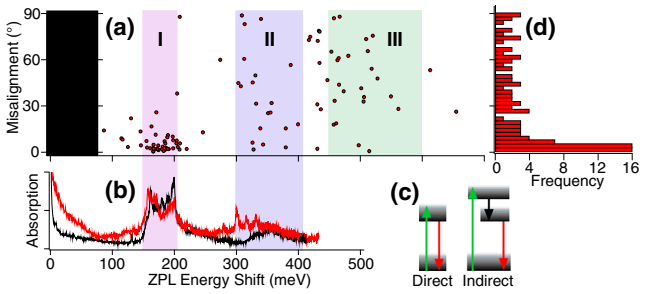

FIG. 3. (a) Scatter plot relating the misalignment angle between the absorption and emission dipole of a ZPL ($\Delta\theta$) to its energy shift from the exciting light (ΔE) for 103 defects. The black box represents ZPL energies that could not be studied due to our selection of optical filters. The shaded region labeled "I" corresponds to the energies of in-plane optical phonons and points in this region are clustered near $\Delta\theta = 0$. ZPLs in regions II and III may be excited via the creation of two and three in-plane optical phonons, respectively. (b) The theoretical absorption band, $W(\Delta E)$, of two defects reveals peaks in regions I and II, verifying that in-plane optical phonons are relevant for absorption and emission. (c) Two energy level diagrams illustrating direct (left) and indirect (right) excitation mechanisms. The left diagram is equivalent to Fig. 1(a) and predicts $\Delta\theta = 0$ whereas the right diagram allows for a broad $\Delta\theta$ distribution. (d) Histogram of all $\Delta\theta$ values shown in (a).

which Eq. (1) often fails. We now frame this critical energy in terms of $F_n^{n^*}$ and the HBN bulk phonon density of states.

At cryogenic temperatures the absorption band $W(E)$ resulting from a single phonon mode is related to the Frank-Condon factor by the expression $W(E) \approx W_0 \sum_{n^*} F_0^{n^*} f(E, n^*)$, where W_0 is the oscillator strength and $f(E, n^*)$ is the line shape of the n^*-phonon sideband. In Fig. 3(b) we plot the theoretical $W(\Delta E)$ for two of the defects investigated. To determine $W(\Delta E)$ we first converted the experimentally measured luminescence spectrum $I_{\text{emit}}(E)$ to its associated emission band by the conversion factor E^{-3} that accounts for the energy-dependent density of optical states [50]. Assuming linear phonon modes, we obtain $W(E)$ by reflecting the emission band about E_{ZPL}. To enable direct comparison with Fig. 3(a), we finally shift $W(E)$ by $-E_{\text{ZPL}}$ to obtain $W(\Delta E)$. This comparison is meaningful because, for defects whose absorption is described by Eq. (1), $W(\Delta E)$ approximates how strongly a ZPL with a particular energy shift will couple to the exciting light. Evidently, the regions of strongest absorption correspond to energy shifts of ~160–200 meV. Figure 3(a) indicates that defects with a ZPL in this spectral range are well described by the Huang-Rhys model.

Here we compare the energies just identified to the relevant bulk phonon energies in HBN [51]. The lowest energy modes are acoustic phonons, and we have shown previously that in-plane acoustic phonons exponentially broaden defect emission in the vicinity of the ZPL as temperature is increased [33]. Consequently, acoustic phonons are relevant for the optical properties of defects in HBN. However, acoustic phonons in HBN range in energy from ~0–107 meV, and are likely not the dominant mode responsible for the absorption band peaks evident in Fig. 3(b). Optical phonon energies, on the other hand, extend from ~72–203 meV and are therefore strong candidates for phonon-mediated absorption and emission. Specifically, out-of-plane optical phonons range in energy from ~72–145 meV whereas in-plane optical phonons range from ~150–203 meV. Only the energies of in-plane optical phonons match the energies identified earlier in Figs. 3(a) and 3(b). To aid in visualizing these energies we have highlighted three regions labeled I–III in Figs. 3(a) and 3(b) that correspond to the absorption band of one, two, and three in-plane optical phonons, respectively. Note that only in region I is the Huang-Rhys model successful, consistent with the low Huang-Rhys factors reported previously [33,42].

Here we propose a mechanism to explain the broad $\Delta\theta$ distribution that incorporates, rather than contradicts, the model presented earlier. In Fig. 1(a) direct absorption between two electronic states is mediated by lattice phonons. This scenario of direct absorption is again depicted on the left of Fig. 3(c), where the vibronic states of the lattice are represented as a blurred continuum. Alternatively, the two electronic states that produce a ZPL may be coupled indirectly via an intermediate electronic state [Fig. 3(c), right] that can be intrinsic to the defect or originate from a neighboring defect. Here transitions between any pair of electronic states are still described by the Huang-Rhys model. However, because the electronic states coupled by the exciting light differ from those that produce the ZPL, we no longer anticipate $\Delta\theta = 0°$.

Although the indirect absorption mechanism correctly predicts a broader $\Delta\theta$ distribution, it does not predict the shape of the distribution, shown in Fig. 3(d). Specifically, if the electronic states are crystallographically related, group theoretic considerations [25,52] predict $\Delta\theta = 0°$ for direct absorption and $\Delta\theta \in \{0°, 30°, 60°, 90°\}$ for indirect absorption. Figure 3(d) does not reveal clustering at these values but rather suggests a flat distribution with clustering at 0°. We propose two explanations for this disagreement. First, we note that our measurement of $\theta_{\text{abs}}(E_{\text{ZPL}})$ and $\theta_{\text{emit}}(E_{\text{ZPL}})$ is only sensitive to the projection of the absorption and emission dipole into the plane of the substrate. Consequently, because the HBN flakes we investigated are often tilted relative to the substrate (see Supplemental Material [49]), the $\Delta\theta$ we measure can differ from the true dipole misalignment. Secondly, it is possible that direct and indirect absorption mechanisms may coexist. In this scenario $\theta_{\text{emit}}(E_{\text{ZPL}})$ is related to the true emission dipole orientation and $\theta_{\text{abs}}(E_{\text{ZPL}})$ is actually a weighted average over all absorption mechanisms. To test whether a particular ZPL may originate from two distinct mechanisms, we acquired spectrally resolved polarization measurements using both 532 and 473 nm light for excitation. Figure 4(a) is a magnified view of a ZPL at ~577 nm excited using 532 (green trace) and 473 nm (blue trace) light, corresponding to energy shifts of ~182 and ~472 meV, respectively. The two spectra overlap well, verifying that each wavelength may

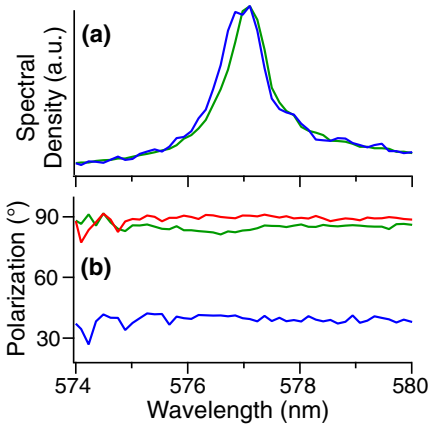

FIG. 4. (a) Emission spectrum of a ZPL at ~577 nm excited with 473 (blue trace) and 532 nm (green trace) light indicating that both energies may excite the transition. (b) Spectrally resolved polarization measurements of $\theta_{\text{abs}}(E)$ for excitation with 532 nm light (green trace) and $\theta_{\text{emit}}(E)$ (red trace) reveal that $\Delta\theta(E_{\text{ZPL}}) \approx 0$. The analogous measurement using 473 nm excitation (blue trace) indicates a large misalignment between the 473 nm absorption dipole and the emission dipole.

excite the same ZPL. In Fig. 4(b) we plot $\theta_{\mathrm{emit}}(E)$ (red trace), $\theta_{\mathrm{abs}}(E)$ for 532 nm excitation (green trace), and $\theta_{\mathrm{abs}}(E)$ for 473 nm excitation (blue trace). Incidentally, $\Delta\theta \approx 0°$ for 532 nm excitation and $\Delta\theta \approx 50°$ for 473 nm excitation. For this defect, the 532 nm excitation is well described by direct absorption whereas the 473 nm excitation is explained by indirect absorption. Therefore, a particular ZPL may be excited via multiple mechanisms.

In conclusion, we made polarization measurements of absorption and emission for 103 isolated defects in HBN with ZPLs in the range ~550–740 nm. In contrast to the predictions of a Huang-Rhys model involving two electronic states, our survey reveals that the absorption and emission dipoles are frequently misaligned. We frame the dipole misalignment $\Delta\theta$ in the context of the energy difference between a ZPL and the exciting light (ΔE), rather than the ZPL energy, and demonstrate that ΔE is a strong indicator of the likelihood that the absorption and emission dipoles are parallel. In particular, if ΔE coincides with an allowed phonon energy in HBN then $\Delta\theta \approx 0°$. Therefore, direct absorption mediated by the creation of a single phonon is efficient and well described by the Huang-Rhys model with two electronic states. Alternatively, if ΔE exceeds the maximum phonon energy in HBN then $0° \leq \Delta\theta \leq 90°$. We propose a mechanism to explain these observations whereby a defect may be excited indirectly through a third intermediate electronic state. This mechanism is supported by polarization measurements acquired using 532 and 473 nm excitation, which reveal that multiple mechanisms may excite a particular ZPL. These comprehensive results form a key advancement in our understanding of absorption and emission mechanisms in HBN single defects.

We thank Brian Calderon for acquiring scanning electron microscope images of annealed HBN flakes. This work was supported by the National Science Foundation (Grant No. DMR-1254530). We acknowledge use of the Cornell NanoScale Facility, a member of the National Nanotechnology Coordinated Infrastructure (NNCI), which is supported by the National Science Foundation (Grant No. ECCS-15420819). Additionally, we acknowledge the Cornell Center for Materials Research Shared Facilities, which are supported through the NSF MRSEC program (Grant No. DMR-1120296).

*Corresponding author.
gdf9@cornell.edu

[1] J. R. Weber, W. F. Koehl, J. B. Varley, A. Janotti, B. B. Buckley, C. G. Van de Walle, and D. D. Awschalom, Proc. Natl. Acad. Sci. U.S.A. **107**, 8513 (2010).
[2] H. Bernien, B. Hensen, W. Pfaff, G. Koolstra, M. S. Blok, L. Robledo, T. H. Taminiau, M. Markham, D. J. Twitchen, L. Childress, and R. Hanson, Nature (London) **497**, 86 (2013).
[3] D. M. Toyli, C. F. de las Casas, D. J. Christle, V. V. Dobrovitski, and D. D. Awschalom, Proc. Natl. Acad. Sci. U.S.A. **110**, 8417 (2013).
[4] J. M. Taylor, P. Cappellaro, L. Childress, L. Jiang, D. Budker, P. R. Hemmer, A. Yacoby, R. Walsworth, and M. D. Lukin, Nat. Phys. **4**, 810 (2008).
[5] A. Sipahigil, M. L. Goldman, E. Togan, Y. Chu, M. Markham, D. J. Twitchen, A. S. Zibrov, A. Kubanek, and M. D. Lukin, Phys. Rev. Lett. **108**, 143601 (2012).
[6] C. Kurtsiefer, S. Mayer, P. Zarda, and H. Weinfurter, Phys. Rev. Lett. **85**, 290 (2000).
[7] R. Brouri, A. Beveratos, J.-P. Poizat, and P. Grangier, Opt. Lett. **25**, 1294 (2000).
[8] Kai-Mei C. Fu, C. Santori, P. E. Barclay, L. J. Rogers, N. B. Manson, and R. G. Beausoleil, Phys. Rev. Lett. **103**, 256404 (2009).
[9] D. A. Simpson, E. Ampem-Lassen, B. C. Gibson, S. Trpkovski, F. M. Hossain, S. T. Huntington, A. D. Greentree, L. C. L. Hollenberg, and S. Prawer, Appl. Phys. Lett. **94**, 203107 (2009).
[10] W. B. Gao, A. Imamoglu, H. Bernien, and R. Hanson, Nat. Photonics **9**, 363 (2015).
[11] B. Hensen, H. Bernien, A. E. Dréau, A. Reiserer, N. Kalb, M. S. Blok, J. Ruitenberg, R. F. L. Vermeulen, R. N. Schouten, C. Abellán, W. Amaya, V. Pruneri, M. W. Mitchell, M. Markham, D. J. Twitchen, D. Elkouss, S. Wehner, T. H. Taminiau, and R. Hanson, Nature (London) **526**, 682 (2015).
[12] E. Barkai, Y. Jung, and R. Silbey, Annu. Rev. Phys. Chem. **55**, 457 (2004).
[13] T. Basché, *Single-Molecule Optical Detection, Imaging and Spectroscopy* (VCH, Weinheim, Cambridge, 1997).
[14] W. F. Koehl, B. B. Buckley, F. J. Heremans, G. Calusine, and D. D. Awschalom, Nature (London) **479**, 84 (2011).
[15] S. Castelletto, B. C. Johnson, V. Ivády, N. Stavrias, T. Umeda, A. Gali, and T. Ohshima, Nat. Mater. **13**, 151 (2013).
[16] M. Widmann, S.-Y. Lee, T. Rendler, N. T. Son, H. Fedder, S. Paik, L.-P. Yang, N. Zhao, S. Yang, I. Booker, A. Denisenko, M. Jamali, S. A. Momenzadeh, I. Gerhardt, T. Ohshima, A. Gali, E. Janzén, and J. Wrachtrup, Nat. Mater. **14**, 164 (2014).
[17] D. J. Christle, A. L. Falk, P. Andrich, P. V. Klimov, J. U. Hassan, N. T. Son, E. Janzén, T. Ohshima, and D. D. Awschalom, Nat. Mater. **14**, 160 (2014).
[18] F. Fuchs, B. Stender, M. Trupke, D. Simin, J. Pflaum, V. Dyakonov, and G. V. Astakhov, Nat. Commun. **6**, 7578 (2015).
[19] B. Lienhard, T. Schröder, S. Mouradian, F. Dolde, T. T. Tran, I. Aharonovich, and D. Englund, Optica **3**, 768 (2016).
[20] A. Lohrmann, B. C. Johnson, J. C. McCallum, and S. Castelletto, Rep. Prog. Phys. **80**, 034502 (2017).
[21] A. J. Morfa, B. C. Gibson, M. Karg, T. J. Karle, A. D. Greentree, P. Mulvaney, and S. Tomljenovic-Hanic, Nano Lett. **12**, 949 (2012).
[22] N. R. Jungwirth, Y. Y. Pai, H. S. Chang, E. R. MacQuarrie, K. X. Nguyen, and G. D. Fuchs, J. Appl. Phys. **116**, 043509 (2014).

[23] S. Choi, B. C. Johnson, S. Castelletto, C. Ton-That, M. R. Phillips, and I. Aharonovich, Appl. Phys. Lett. **104**, 261101 (2014).
[24] O. Neitzke, A. Morfa, J. Wolters, A. W. Schell, G. Kewes, and O. Benson, Nano Lett. **15**, 3024 (2015).
[25] N. R. Jungwirth, H.-S. Chang, M. Jiang, and G. D. Fuchs, ACS Nano **10**, 1210 (2016).
[26] S. Ghosh, M. Ghosh, M. Seibt, and G. Mohan Rao, Nanoscale **8**, 2632 (2016).
[27] A. M. Berhane, K.-Y. Jeong, Z. Bodrog, S. Fiedler, T. Schröder, N. V. Triviño, T. Palacios, A. Gali, M. Toth, D. Englund, and I. Aharonovich, Adv. Mater. **29**, 1605092 (2017).
[28] M. Koperski, K. Nogajewski, A. Arora, V. Cherkez, P. Mallet, J.-Y. Veuillen, J. Marcus, P. Kossacki, and M. Potemski, Nat. Nanotechnol. **10**, 503 (2015).
[29] Y.-M. He, G. Clark, J. R. Schaibley, Y. He, M.-C. Chen, Y.-J. Wei, X. Ding, Q. Zhang, W. Yao, X. Xu, C.-Y. Lu, and J.-W. Pan, Nat. Nanotechnol. **10**, 497 (2015).
[30] C. Chakraborty, L. Kinnischtzke, K. M. Goodfellow, R. Beams, and A. N. Vamivakas, Nat. Nanotechnol. **10**, 507 (2015).
[31] T. T. Tran, S. Choi, J. A. Scott, Z. Xu, C. Zheng, G. Seniutinas, A. Bendavid, M. S. Fuhrer, M. Toth, and I. Aharonovich, arXiv:1701.00041.
[32] T. T. Tran, K. Bray, M. J. Ford, M. Toth, and I. Aharonovich, Nat. Nanotechnol. **11**, 37 (2015).
[33] N. R. Jungwirth, B. Calderon, Y. Ji, M. G. Spencer, M. E. Flatté, and G. D. Fuchs, Nano Lett. **16**, 6052 (2016).
[34] T. T. Tran, C. Elbadawi, D. Totonjian, C. J. Lobo, G. Grosso, H. Moon, D. R. Englund, M. J. Ford, I. Aharonovich, and M. Toth, ACS Nano **10**, 7331 (2016).
[35] Z. Shotan, H. Jayakumar, C. R. Considine, M. Mackoit, H. Fedder, J. Wrachtrup, A. Alkauskas, M. W. Doherty, V. M. Menon, and C. A. Meriles, ACS Photonics **3**, 2490 (2016).
[36] L. J. Martínez, T. Pelini, V. Waselowski, J. R. Maze, B. Gil, G. Cassabois, and V. Jacques, Phys. Rev. B **94**, 121405 (2016).
[37] N. Chejanovsky, M. Rezai, F. Paolucci, Y. Kim, T. Rendler, W. Rouabeh, F. Fávaro de Oliveira, P. Herlinger, A. Denisenko, S. Yang, I. Gerhardt, A. Finkler, J. H. Smet, and J. Wrachtrup, Nano Lett. **16**, 7037 (2016).
[38] A. W. Schell, T. T. Tran, H. Takashima, S. Takeuchi, and I. Aharonovich, APL Photonics **1**, 091302 (2016).
[39] G. Grosso, H. Moon, B. Lienhard, S. Ali, D. K. Efetov, M. M. Furchi, P. Jarillo-Herrero, M. J. Ford, I. Aharonovich, and D. Englund, arXiv:1611.03515.
[40] A. W. Schell, H. Takashima, T. T. Tran, I. Aharonovich, and S. Takeuchi, arXiv:1701.02696.
[41] M. Kianinia, B. Regan, S. A. Tawfik, T. T. Tran, M. J. Ford, I. Aharonovich, and M. Toth, ACS Photonics **4**, 768 (2017).
[42] A. L. Exarhos, D. A. Hopper, R. R. Grote, A. Alkauskas, and L. C. Bassett, ACS Nano **11**, 3328 (2017).
[43] T. T. Tran, D. Wang, Z.-Q. Xu, A. Yang, M. Toth, T. W. Odom, and I. Aharonovich, Nano Lett. **17**, 2634 (2017).
[44] R. Bourrellier, S. Meuret, A. Tararan, O. Stéphan, M. Kociak, L. H. G. Tizei, and A. Zobelli, Nano Lett. **16**, 4317 (2016).
[45] M. Abdi, M.-J. Hwang, M. Aghtar, and M. B. Plenio, arXiv:1704.00638.
[46] K. Huang and A. Rhys, P. Roy. Soc. A: Math. Phys. **204**, 406 (1950).
[47] J. T. Ritter and J. J. Markman, Phys. Rev. **185**, 1201 (1969).
[48] A. M. Stoneham, *Theory of Defects in Solids: Electronic Structure of Defects in Insulators and Semiconductors* (Oxford University Press, Oxford, 2001).
[49] See Supplemental Material at http://link.aps.org/supplemental/10.1103/PhysRevLett.119.057401 for experimental apparatus and spectrally-averaged polarization measurements; Spectrally-resolved polarization measurements; Sample details; Lifetime distribution; Visibility distribution.
[50] M. de Jong, L. Seijo, A. Meijerink, and F. T. Rabouw, Phys. Chem. Chem. Phys. **17**, 16959 (2015).
[51] T. Tohei, A. Kuwabara, F. Oba, and I. Tanaka, Phys. Rev. B **73**, 064304 (2006).
[52] M. S. Dresselhaus, G. Dresselhaus, and A. Jorio, *Group Theory: Application to the Physics of Condensed Matter* (Springer Berlin Heidelberg, 2007).